

## Astrospheres, stellar winds, and the interstellar medium

BRIAN E. WOOD AND JEFFREY L. LINSKY

### 3.1 The spatial extent of the solar wind

While orbiting the Sun, the Earth and the other planets in our solar system are exposed to an outflow of plasma from the Sun. This is the solar wind, which largely determines the particle environment of the planets, as well as their magnetospheric properties. Long-term exposure to the solar wind may have had significant effects on planetary atmospheres in some cases. Mars is a particularly interesting example, as the Martian atmosphere was once much thicker than it is today, and the erosive effects of solar wind exposure are commonly believed to be responsible for its depletion (see Ch. 8; also Jakosky *et al.*, 1994; Atreya *et al.*, 2013).

The solar wind does not expand indefinitely. Eventually it runs into the interstellar medium (ISM), the extremely low-particle-density environment that exists in between the stars. Our Sun is moving relative to the ISM that surrounds the planetary system, so we see a flow of interstellar matter in the heliocentric rest frame, coming from the direction of the constellation Ophiuchus. The interaction between the solar wind and the ISM flow determines the large-scale structure of our heliosphere, which basically defines the extent of the solar wind's reach into our Galactic environment. Other stars are naturally surrounded by their own "astrospheres" (alternatively "asterospheres") defined by the strength of their own stellar winds, the nature of the ISM in their Galactic neighborhoods, and their relative motion.

Much as the Earth's magnetosphere plays a role in protecting the Earth's atmosphere from direct and potentially damaging exposure to the solar wind, the global heliosphere has its own role to play in shielding the planets that exist inside it from high-energy particles, called Galactic Cosmic Rays (GCRs), that permeate the Galaxy (see Vol. II, Ch. 9; and Vol. III, Ch. 9). Some of these GCRs do penetrate into the inner heliosphere and encounter Earth. The extent to which they have influenced our planet and the evolution of life is debatable, but cosmic rays cause radiation damage and mutations in DNA (Dartnell, 2011). There are also claims

that cosmic rays may be involved in atmospheric processes such as lightning formation and cloud formation (Carslaw *et al.*, 2002; Shaviv, 2005a; Svensmark *et al.*, 2009). In any case, the global heliosphere does reduce the fluxes of GCRs that reach Earth and other planets, providing some level of protection from GCR influence within the solar system.

Given their effects on planets in our solar system, including Earth, it is of interest to understand how the solar wind and heliosphere have changed during the course of the Sun's 4.6 billion year lifetime. Likewise, it is also important to understand the evolution of stellar winds and their effect on exoplanets. Not only does the solar wind evolve as the Sun ages, but the Sun encounters different ISM environments as it orbits the Galactic Center, leading to changes in heliospheric structure. The focus of this chapter is on describing the evolution of the solar wind and heliosphere, or more generally stellar winds and astrospheres, on these very long timescales. We begin by describing what is known about the current structure and extent of our heliosphere.

### 3.2 Observed properties of the local interstellar medium

The structure of our heliosphere depends on the properties of both the solar wind and the surrounding ISM. The basic properties of the hot and fully ionized solar wind are described in other chapters in the Heliophysics book series (cf., Table 1.2), such as in Ch. 9 in Vol. I. In this section we describe what we know about the ISM surrounding the Sun.

Our knowledge of the local ISM is based on observations of high-resolution spectra of nearby stars that contain absorption lines produced by interstellar gas, and on measurements of interstellar gas entering the heliosphere. An example of absorption line data is shown in Fig. 3.1, where these particular data are UV spectra from the *Hubble Space Telescope* (HST). Absorption towards the nearby star 36 Oph is shown from singly ionized Mg and Fe atoms (the spectra of which are referred to as Mg II and Fe II), and from neutral deuterium (D I). Crutcher (1982) first noticed that the radial velocities of interstellar absorption lines in the spectra of nearby stars are consistent with interstellar gas flowing toward the Sun from the direction of the Scorpio–Centaurus Association. Subsequent investigations (e.g., Lallement and Bertin, 1992; Frisch *et al.*, 2002) found that the interstellar gas flow has a number of components with slightly different flow directions and speeds. Redfield and Linsky (2008) identified 15 different velocity components, which they called clouds, by analyzing interstellar absorption lines in HST spectra of 157 stars located within 15 parsecs (pc) of the Sun.

The sky map in Fig. 3.2 shows the locations of four of the closest clouds. The Local Interstellar Cloud (LIC) is so-named because it occupies nearly half of the

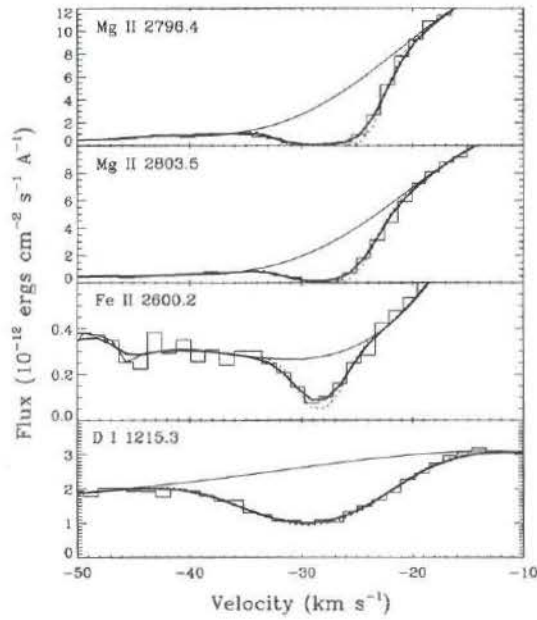


Fig. 3.1 High-resolution spectra of the star 36 Oph showing interstellar absorption in Mg II, Fe II, and D I lines, with wavelengths provided in ångström ( $\text{\AA}$ ) units. The spectra are plotted in a heliocentric rest frame. Note the different absorption widths, with D I being broadest due to deuterium atoms having the lowest mass and therefore the highest thermal speeds. (From Wood *et al.*, 2000.)

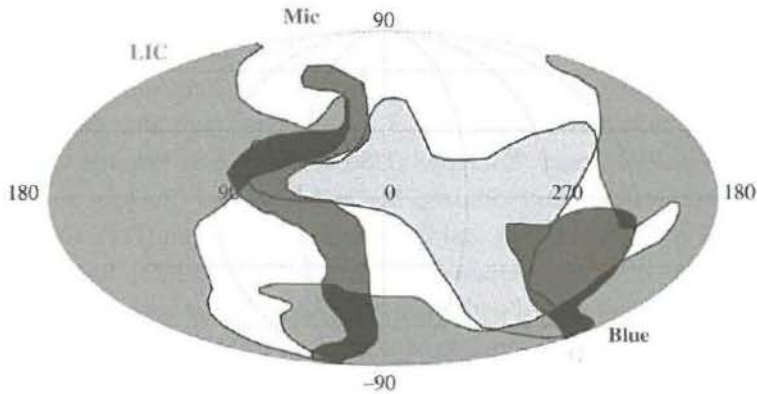


Fig. 3.2 Map in Galactic coordinates of the four partially ionized warm interstellar clouds that are closest to the Sun, mapped using ISM absorption lines. The Sun is likely located inside of the Local Interstellar Cloud (LIC), but very near the edge, explaining why LIC absorption is not detectable in all directions and therefore the ISM absorption lines by the LIC do not fill the sky. (From Redfield and Linsky, 2008.)

sky, implying that the Sun is located just inside of the LIC or immediately outside. The decision as to which option is more likely true requires the second type of data: measurements of interstellar gas flowing into the heliosphere as described below. The second largest cloud by angular area is the G cloud, so-named because it is centered in the Galactic Center direction. The line of sight to  $\alpha$  Centauri, the nearest star to the Sun at a distance of 1.3 pc, shows interstellar absorption only at the projected velocity of the G-cloud vector with no absorption at the LIC cloud velocity. The upper limit of the neutral hydrogen (H I) column density (the total number of atoms or ions between the source and the telescope per unit cross section) at the LIC velocity in this direction indicates that the Sun will leave the LIC in less than 3000 years if it has not already done so. The Blue Cloud is also very near because absorption at the projected velocity of its flow vector is seen toward the star Sirius (at 2.6 pc). Finally, the nearby Mic Cloud shows a filamentary structure that may be typical of many clouds. A further question is whether the picture of discrete interstellar clouds described by Redfield and Linsky (2008) is the best representation of the interstellar kinematics or whether a single cloud with a continuous gradient in flow velocity is a more realistic model for the interstellar gas surrounding the Sun. Gry and Jenkins (2014) provide arguments for a continuous flow pattern rather than many discrete clouds, but Redfield and Linsky (2015) argue that the discrete cloud model best fits the data.

Absorption line data like those in Fig. 3.1 provide measurements of ISM column densities, projected flow velocities onto the line of sight, and Doppler width parameters ( $b$ ). The column densities provide one crucial indication of ISM density outside the heliosphere for various atomic species. Electron (and hence proton) density can be estimated by certain density sensitive line ratios (Frisch, 1994; Wood and Linsky, 1997; Redfield and Falcon, 2008). The Doppler parameters can be related to temperature ( $T$ ) and non-thermal speed ( $\xi$ ) through the equation

$$b^2 = \frac{2kT}{m} + \xi^2, \quad (3.1)$$

where  $k$  is the Boltzmann constant and  $m$  is the mass of the atomic species in question. Note the broader width of the D I line in Fig. 3.1 compared to the heavier species Mg II and Fe II. Measurements of  $b$  from different species with different masses (and hence different thermal widths) can provide measurements of  $T$  and  $\xi$ , as shown explicitly in Fig. 3.3.

Besides absorption data, the other principle sources of direct information about the ISM properties in the solar neighborhood are observations of neutral ISM species streaming through the solar system with hardly any collisional interactions. Most important are observations of neutral He from particle detectors on the *Ulysses* spacecraft, which operated from 1990 until 2007 (e.g., Witte, 2004), and on the later *Interstellar Boundary Explorer (IBEX)* mission (e.g., McComas

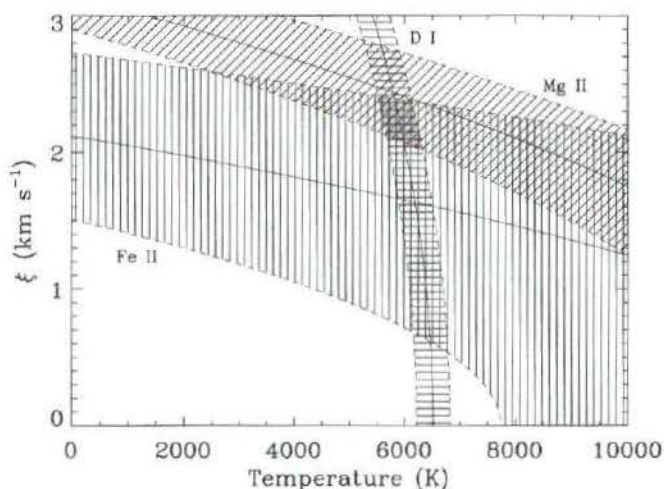


Fig. 3.3 Non-thermal ISM speeds ( $\xi$ ; see Eq. (3.1)) plotted versus temperature, based on the Doppler width parameters measured from the lines in Fig. 3.1. The shaded area where the three curves overlap indicates the best temperature and  $\xi$  value. (From Wood *et al.*, 2000.)

*et al.*, 2012); and observations of neutral H in the inner solar system from Lyman- $\alpha$  backscatter measurements (e.g., Lallement *et al.*, 2005).

Based largely on the observational constraints described above, the ISM flow speed in the solar rest frame is known to be in the range  $v_{\text{ISM}} = 23\text{--}27 \text{ km s}^{-1}$ , and the temperature is  $T = 6000\text{--}9000 \text{ K}$ . The dominant constituents of the ISM by mass and number are protons and neutral hydrogen atoms, and typical estimates of proton and neutral hydrogen densities are  $n_p \approx 0.06 \text{ cm}^{-3}$  and  $n_H \approx 0.18 \text{ cm}^{-3}$  (e.g., Müller *et al.*, 2008; Slavin and Frisch, 2008; Frisch *et al.*, 2011).

### 3.3 Introduction to heliospheric structure

Speculation about the nature of the heliosphere's structure began shortly after the solar wind was first discovered (Parker, 1961). Figure 3.4 shows the prevailing picture of the global heliosphere that has existed for several decades (Holzer, 1989; Zank, 1999). The structure is characterized by three flow discontinuities: the termination shock (TS), the heliopause (HP), and the bow shock (BS). The solar wind density and therefore its ram pressure fall off as  $r^{-2}$ , where  $r$  is the distance from the Sun. The wind speed is supersonic and super-Alfvénic, so when the ram pressure falls to the pressure of the ambient ISM, the result is a shock, specifically the ellipsoidal TS in Fig. 3.4, where the flow is decelerated.

If the ISM flow is super-Alfvénic, it also encounters a shock as it approaches the Sun, specifically the roughly hyperboloid shaped BS in Fig. 3.4, where the

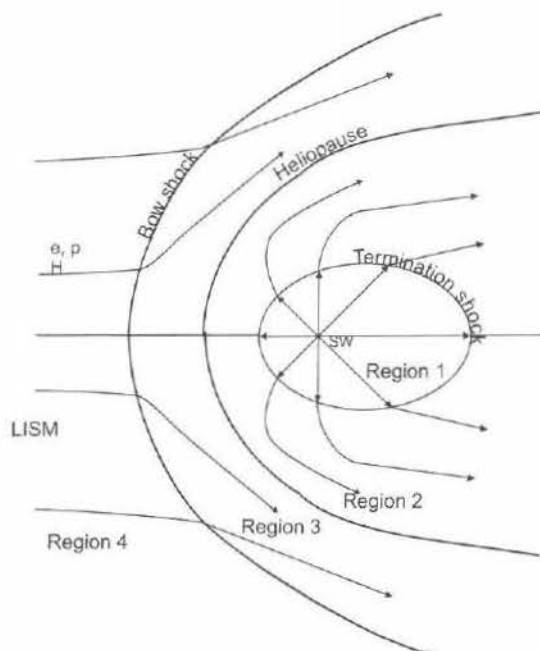


Fig. 3.4 Basic structure of the global heliosphere, with three discontinuities: the termination shock (TS), heliopause (HP), and bow shock (BS). These discontinuities separate the heliosphere into four regions, with significantly different plasma properties: (1) supersonic solar wind; (2) decelerated, heated, and deflected solar wind; (3) decelerated, heated, and deflected ISM; and (4) undisturbed local ISM (LISM) flow, here assumed supersonic, resulting in a bow shock. (From Izmodenov *et al.*, 2002.)

ISM flow is decelerated to subsonic speeds. However, the  $v_{\text{ISM}} = 23\text{--}27 \text{ km s}^{-1}$  interstellar flow happens to yield an Alfvénic Mach number of  $M_A \approx 1$ , making the existence or nonexistence of a BS very much an open question. Much depends on the strength and orientation of the ISM magnetic field,  $B_{\text{ISM}}$ . The higher  $B_{\text{ISM}}$  is (and the more perpendicular to the ISM flow), the lower  $M_A$  should be, and less likely that there is a bow shock.

Even the seemingly small uncertainty in  $v_{\text{ISM}}$  is enough to make a difference. For many years the best assessments were believed to be the  $v_{\text{ISM}} = 26.3 \pm 0.4 \text{ km s}^{-1}$  measurement of the ISM neutral He flowing through the solar system by *Ulysses* (Witte, 2004) and the  $v_{\text{ISM}} = 25.7 \pm 0.5 \text{ km s}^{-1}$  measurement of Lallement and Bertin (1992) from ISM absorption lines. With these relatively high values, heliospheric modelers favored  $M_A > 1$ , implying the existence of a BS. However, later He flow measurements and a new analysis of ISM absorption line data have yielded lower velocities. Specifically, measurements of neutral He flow from *IBEX* suggest

$v_{\text{ISM}} = 23.2 \pm 0.3 \text{ km s}^{-1}$  (McComas *et al.*, 2012), and Redfield and Linsky (2008) find  $v_{\text{ISM}} = 23.84 \pm 0.90 \text{ km s}^{-1}$  from ISM absorption lines.

This has been enough for many to argue that  $M_A < 1$  should be preferred (McComas *et al.*, 2012; Zieger *et al.*, 2013), though Scherer and Fichtner (2014) argue that including  $\text{He}^+$  density in the calculation of sound and Alfvén speeds instead of just assuming a pure proton plasma would still suggest  $M_A > 1$  even if  $v_{\text{ISM}} \approx 23 \text{ km s}^{-1}$ . With  $M_A$  so close to 1, it is possible that the issue will not be fully resolved until an interstellar probe mission of some sort is sent out to this region (McNutt *et al.*, 2004). However, with  $M_A$  so close to 1 it is also possible that secondary physical processes (e.g., charge-exchange interactions with neutral particles) make it fundamentally ambiguous whether any boundary that may exist out there should be called a true BS, or whether we should instead refer to it as a “bow wave” (Zank *et al.*, 2013).

Regardless of whether or not a bow shock exists, strong plasma interactions prevent the ISM plasma from mixing with the solar-wind plasma. The roughly paraboloid heliopause in Fig. 3.4, lying between the termination shock and the bow shock (or wave) is the contact discontinuity separating the two plasma flows. Representing the boundary between solar wind and ISM plasma, the heliopause is generally considered the true boundary of the heliosphere.

### 3.4 Observational constraints on the global heliosphere

Until relatively recent times, the heliospheric structure shown in Fig. 3.4 was a purely theoretical one, with few observational constraints to test models of this structure. This changed dramatically on 2004 December 16 when *Voyager 1* crossed the TS at a distance of  $r = 94$  Sun–Earth distances (astronomical units, or AU; Stone *et al.*, 2005). The two *Voyager* spacecraft, *Voyager 1* (V1) and *Voyager 2* (V2), were launched in 1977. After exploring the outer planets, both ended up in advantageous trajectories roughly in the upwind direction of the heliosphere (relative to the ISM flow), allowing them to cross the TS while still operational, and probe regions of the heliosphere never before explored. However, V1’s identification of the TS crossing was not trivial. The instrument on the spacecraft designed to study the ambient bulk plasma failed in 1980, limiting V1’s diagnostics of its plasma environment to those provided by its magnetometer, and instruments designed to study energetic particles and plasma waves. In 2002, V1 began seeing enhancements in energetic particles that created uncertainty as to whether the TS had been crossed (Krimigis *et al.*, 2003) but, with the benefit of hindsight, 2004 December 16 is now considered the true crossing, which came with a clear jump in magnetic field. Thanks in part to the fact that V2 has an operating plasma instrument, V2 observed a less-ambiguous TS crossing on 2007 August 30 at

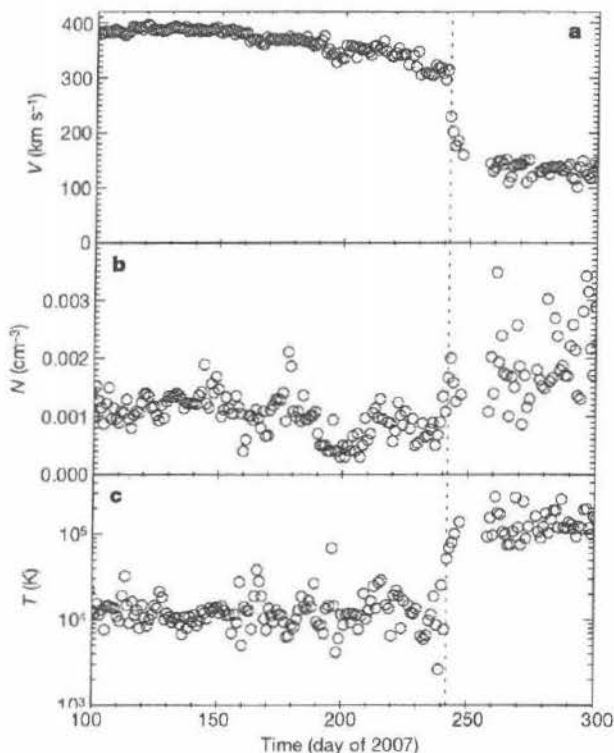


Fig. 3.5 *Voyager 2* observations of solar wind (a) speed, (b) proton number density, and (c) temperature. The dotted line indicates the termination shock (TS) crossing on 2007 August 30 at a distance of 84 AU from the Sun. (From Richardson *et al.*, 2008.)

$r = 84$  AU, which is shown explicitly in Fig. 3.5 (Richardson *et al.*, 2008; Stone *et al.*, 2008).

Much as identifying V1's TS crossing proved problematic, identifying the HP crossing is also proving difficult. On August 25, 2012, at  $r = 122$  AU, V1 observed an increase in magnetic field, a dramatic increase in GCR intensities, and a disappearance of lower energy ions that had been observed since the TS crossing (Stone *et al.*, 2013; see Fig 4.6). Plasma-wave data from V1 have since suggested a substantial increase in plasma density, consistent with this being the HP crossing (Gurnett *et al.*, 2013). This would make V1 the first spacecraft to leave the heliosphere and enter interstellar plasma. However, the lack of any change in magnetic-field direction and the unexpectedly close HP distance have led to alternative, more complex interpretations (Schwadron and McComas, 2013; Borovikov and Pogorelov, 2014). Presumably time and a supporting HP crossing by V2 will ultimately resolve the issue.

The basic structure in Fig. 3.4 is mostly defined by plasma interactions. The local ISM is partly neutral, but collisional mean free paths for neutrals are large compared to the size of the heliosphere, so their effects on heliospheric structure were long ignored. In essence, the assumption was that neutrals pass through the heliosphere unimpeded, feeling only the Sun's gravity and photoionizing flux. However, in reality neutrals do participate in heliospheric interactions through charge exchange (CX). The CX interactions end up providing ways to remotely explore the heliosphere that would be impossible if the local ISM were fully ionized.

A CX interaction is a rather simple process by which an electron hops from a neutral atom to a neighboring ion (e.g.,  $H^0 + H^+ \rightarrow H^+ + H^0$ ). Mean free paths for CX for most neutral ISM atoms are short enough that they do experience significant CX losses on their way through the heliosphere. The exceptions are the noble gases, which have low CX cross sections, explaining why neutral He flowing through the solar system is considered the best local probe of the undisturbed ISM flow (Witte, 2004).

Modeling neutrals in the heliosphere is very difficult because CX sends the neutrals wildly out of thermal and ionization equilibrium with the ambient plasma. Including neutrals in hydrodynamic models of the global heliosphere therefore requires either a fully kinetic treatment of the neutrals, or at least a sophisticated multi-fluid approach. The earliest models that could treat neutrals properly were from the 1990s (Baranov and Malama, 1993, 1995; Zank *et al.*, 1996). These models demonstrated that through CX, neutrals could have significant effects on heliospheric structure. Figure 3.6 shows one of these models (Müller and Zank, 2004). The ISM protons are heated, compressed, deflected, and decelerated as they approach the HP, and thanks to CX the proton properties are at least partially imprinted on the neutral hydrogen (H I) as well, creating what has been called a "hydrogen wall" of higher density H I (see Fig. 3.6) around the heliosphere, in between the HP and BS. The importance of this hydrogen wall is that it is actually detectable in UV spectra from HST, not only around the Sun but around other stars as well.

The effect of heliospheric and astrospheric absorption on stellar H I Lyman- $\alpha$  spectra is described by Fig. 3.7 (Wood, 2004), showing the journey of a Lyman- $\alpha$  photon from the star to the observer. Most of the absorption is by interstellar gas in the line of sight from the star to the Sun, but the astrosphere and heliosphere provide additional absorption on the left and right sides of the interstellar absorption, respectively. The effect of the hydrogen wall around the Sun is to provide additional red-shifted absorption on the right side of the interstellar absorption feature because the neutral hydrogen gas in the solar hydrogen wall is slowed down and deflected relative to the inflowing interstellar gas. Conversely, the absorption by the

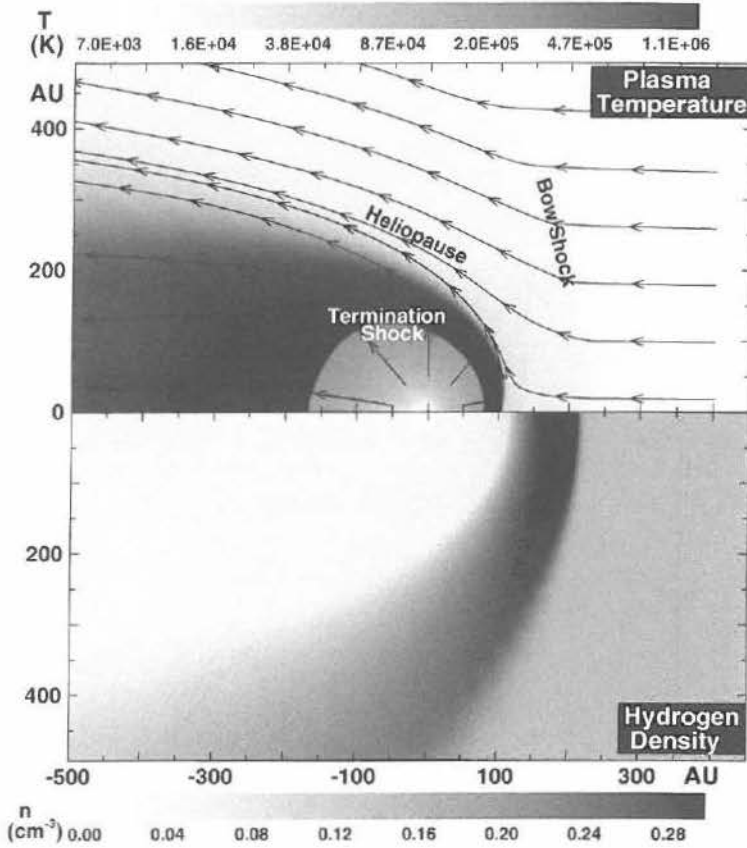


Fig. 3.6 A 2.5D axisymmetric, hydrodynamic model of the heliosphere from Müller and Zank (2004). The upper panel shows plasma temperature, and the bottom panel shows neutral hydrogen density.

hydrogen wall gas around the star is seen as blue-shifted relative to the interstellar flow from our perspective outside the astrosphere, and is therefore seen on the left side of the absorption line. The first detection of hydrogen wall absorption was in HST observations of the two stars in the very nearby binary  $\alpha$  Cen (with spectral types G2 V+K1 V; i.e., with one component very comparable to our Sun also of spectral type G2 V, see, for example, Fig. 2.8 in Vol. III for a Hertzsprung–Russell diagram for spectral type characterization). The bottom panel of Fig. 3.7 shows the H I (and D I) Lyman- $\alpha$  spectrum of the lower-brightness component of this binary, known as  $\alpha$  Cen B (Linsky and Wood, 1996). Most of the intervening H I and D I between us and the star is interstellar, but the ISM cannot account for all of the H I absorption. As mentioned above, the red-shifted excess on the right side is heliospheric and the blue-shifted excess on the left is astrospheric (Gayley *et al.*, 1997).

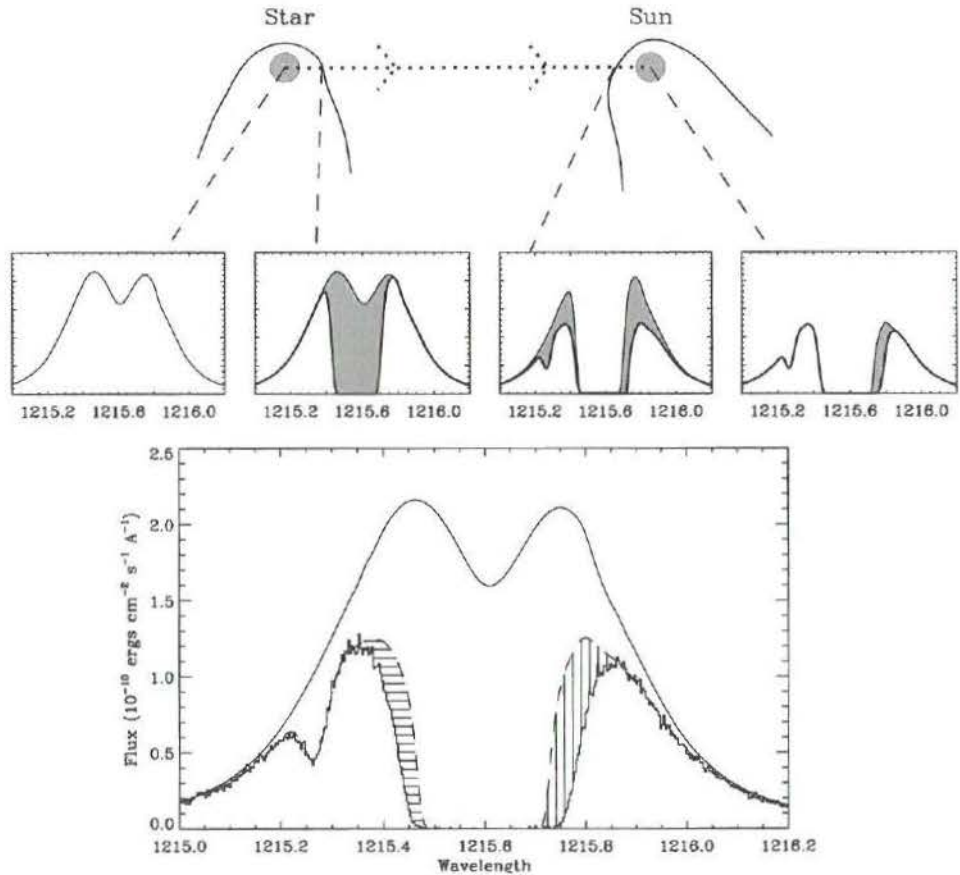


Fig. 3.7 Top panel: the journey of a Lyman- $\alpha$  photon from a star through its astrosphere, the interstellar medium, and the heliosphere. Middle panel from left to right: the Lyman- $\alpha$  emission line emitted by the star, absorption due to the stellar astrosphere, additional absorption due to the interstellar medium, and additional absorption due to the heliosphere. Bottom panel: HST Lyman- $\alpha$  spectrum of  $\alpha$  Cen B, showing broad H I absorption at 1215.6  $\text{\AA}$  and D I absorption at 1215.25  $\text{\AA}$ . The upper solid line is the assumed stellar emission profile and the dashed line is the ISM absorption alone. The excess absorption is due to heliospheric H I (vertical lines) and astrospheric H I (horizontal lines). (From Wood, 2004.)

Besides the hydrogen wall, CX in the heliosphere has other observable consequences. Within the TS, outflowing solar wind plasma can CX with neutral H that penetrates inside the TS, yielding solar-wind neutral H atoms, and inflowing ISM protons that are then picked up by the solar wind. These “pickup ions” (PUIs) create a suprathermal particle population within the solar wind that is energetically very important beyond the orbit of Saturn ( $\sim 10$  AU from the Sun). The PUI

population is energized at the TS. It was long believed that this is the source of anomalous cosmic rays (ACRs) (see Vol. II, Ch. 9), but V1 and V2 found that the ACRs that they observed near the TS were not coming from nearby (Stone *et al.*, 2005). This has led to other suggestions for the source of ACRs somewhere beyond the TS (Fisk and Gloeckler, 2008), but the issue is far from resolved.

The *IBEX* mission, launched in 2008, was designed primarily to study energetic neutral atoms (ENAs) streaming into the solar system from beyond the TS. The globally distributed ENAs observed by *IBEX* are presumed to be created by CX with the post-TS PUI population (Schwadron *et al.*, 2011). Charge exchange with the bulk solar-wind plasma beyond the TS creates a less-energetic population of neutrals that is detectable in HST Lyman- $\alpha$  spectra. In contrast to the hydrogen wall population, which is detectable primarily in upwind directions, it is only in very downwind directions, with very long path lengths through the post-TS region 2 (see Fig. 3.4), that very broad but very weak absorption from the region 2 neutrals can be discerned against the Lyman- $\alpha$  emission from background stars. Detections of this absorption represent the first detection of the heliotail (Wood *et al.*, 2007b, 2014a).

The most unexpected result from *IBEX* does not relate to the neutralized post-TS PUI ENAs but instead to a ribbon of ENA flux that stretches across the sky (McComas *et al.*, 2009). The ribbon's origin is uncertain, but most believe it must be due to heliospheric asymmetries induced by the ISM magnetic field (Heerikhuisen *et al.*, 2010), which is poorly constrained by any direct ISM observations. Modeling heliospheric asymmetries induced by the ISM field requires sophisticated, fully three-dimensional (3D) MHD state-of-the-art models (e.g., Pogorelov *et al.*, 2008; Opher *et al.*, 2009).

### 3.5 Effects of a variable ISM on past heliospheric structure

The Sun is now traveling through the ISM at a rate of 16–20 pc per million years (Myr) compared to the average motion of nearby stars about the Galactic Center. The ISM has densities ranging from  $10^4 \text{ cm}^{-3}$  or higher in dense molecular clouds down to about  $0.005 \text{ cm}^{-3}$  in very-low-density hot-gas regions. Because the heliosphere will contract or expand by large factors when the Sun enters such high- or low-density regions, it is important to investigate when such environmentally driven changes could have occurred and will possibly occur by considering the Sun's historic and future path through the ISM.

At present, the heliosphere resides inside of the partially ionized LIC (see Section 3.2 of this chapter), with properties likely similar to other warm partially ionized clouds within 15 pc of the Sun. The Sun likely entered this cluster of local warm clouds about 1 Myr ago. However, on a larger scale, the Sun actually lies in

a region called the Local Cavity, or Local Bubble, which is  $\sim 200$  pc across and is filled mostly with fully ionized, low density ISM (Welsh *et al.*, 2010; Frisch *et al.*, 2011). Wyman and Redfield (2013) measured the Na I and Ca II column densities towards stars along the path that the Sun has traveled for the past 30 Myr (500 pc). They found no evidence for the Sun having encountered an environment significantly denser than the LIC until about 7.5 Myr ago (120 pc) when the Sun was at the edge of the Local Cavity. If the discrete cloud model of Redfield and Linsky (2008) is accurate, the Sun will soon leave the LIC in less than 3000 yr. What will be the properties of this new environment?

The classic papers of McKee and Ostriker (1977) and Wolfire *et al.* (1995) predict that the ISM should consist of three components: the cold neutral medium ( $T \leq 50$  K), the warm neutral or ionized medium with  $T \sim 8000$  K (e.g., like the LIC), and the million-degree low-density ionized medium. These models assume that the three components coexist in pressure and thermal equilibrium, which is actually unlikely. Numerical simulations by Berghöfer and Breitschwerdt (2002), which include supernova explosions and realistic thermal processes, predict a very wide range of densities and temperatures in the ISM but no pressure equilibrium and no identifiable thermal phases. Observations are needed to determine which of these two very different pictures is more realistic.

The nearby warm partially ionized gas clouds have properties roughly consistent with the warm component (neutral or ionized) predicted by the classic models. Cold dense molecular clouds are observed typically by CO and H I 21-cm emission in many parts of the Galaxy. The nearest cold gas with a temperature of 15–30 K is the Leo cloud located at a distance between 11.3 and 24.3 pc from the Sun (Peek *et al.*, 2011).

Our ideas concerning the properties of the gas located between the warm local ISM clouds have undergone a radical change in the past 20 years. The gas between the clouds, extending out to roughly 100 pc from the Sun in what is now called the Local Cavity was originally assumed to be hot (roughly  $10^6$  K), fully ionized, and low density (roughly  $0.005 \text{ cm}^{-3}$ ). This conclusion was based upon the predictions of the classical models and observations of diffuse soft X-ray emission consistent with the properties of the hot gas. This picture has since been complicated by the realization that X-ray emission from CX reactions between the solar wind ions and inflowing interstellar neutral hydrogen can explain much of the observed diffuse X-ray emission, except for the Galactic pole regions (Cravens, 2000; Koutroumpa *et al.*, 2009). Welsh and Shelton (2009) have instead proposed that the Local Cavity is an old supernova remnant with photoionized gas at a temperature of about 20 000 K. The likely photoionizing sources are the hot stars  $\epsilon$  CMa and  $\beta$  CMa (Vallerga and Welsh, 1995) and nearby hot white dwarfs like Sirius B (Linsky and Redfield, 2014).

How will the heliosphere change as the Sun passes through very different regions of the interstellar medium? To answer this question, Müller *et al.* (2006) computed a set of heliosphere models under the assumption that the solar wind retains its present properties. Figure 3.8 compares today's heliosphere properties with the Sun located inside of the partially ionized warm LIC to a model computed for the Sun surrounded by  $10^6$  K fully ionized interstellar plasma. The main difference between these models is that the hydrogen wall does not exist when the inflowing interstellar gas contains no neutral hydrogen atoms. The locations of the termination shock (TS), heliopause (HS), and bow shock (BS) are determined by pressure balance between the solar-wind ram pressure and the thermal and ram pressure of the surrounding interstellar gas. In this comparison, the locations of the TS, HP, and BS are about the same in the two models because the high temperature and

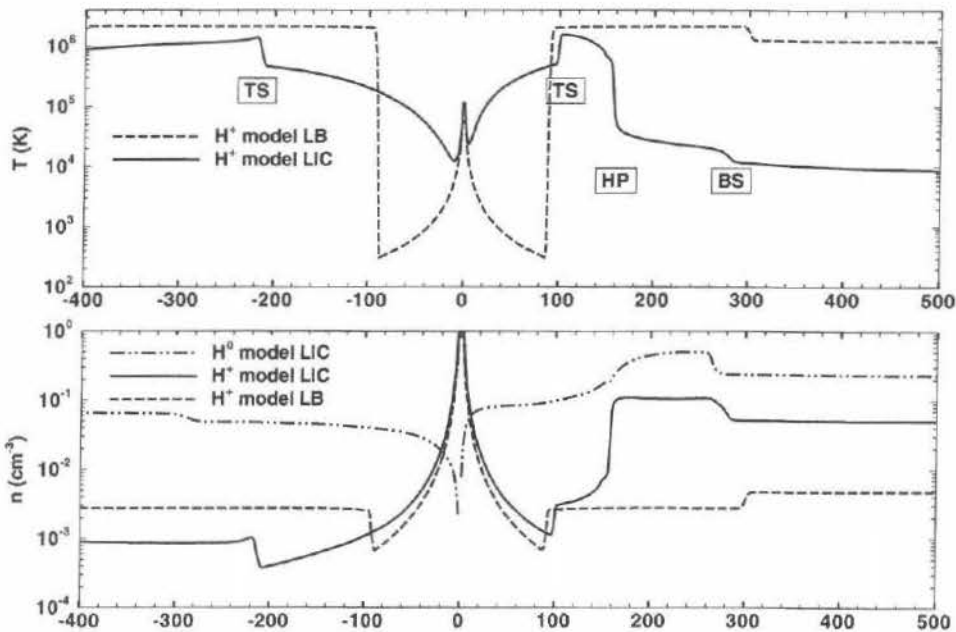


Fig. 3.8 Top: plots of the temperature vs. distance in Sun–Earth distances (astronomical units, or AU) relative to the Sun (interstellar flow upwind direction to the right and downwind to the left) for a heliosphere model with the Sun located inside of the Local Interstellar Cloud (LIC; solid line) or inside a  $10^6$  K hot interstellar medium (dashed line). The heliosphere in the LIC model has a termination shock (TS), heliopause (HP) and bow shock (BS) structure. Bottom: density structures for the LIC neutral hydrogen (solid line), LIC protons (dot-dash line), and hot interstellar model protons (dashed line). Note that the hydrogen wall at 150–280 AU exists when the heliosphere is located inside partially neutral interstellar gas but not when it is inside fully ionized interstellar gas. (Figure from Müller *et al.*, 2009.)

low density of the interstellar gas produce a pressure that is about the same as in the LIC.

When the Sun enters a region of much higher density or speed, and therefore higher ram pressure, the effect is to compress the heliosphere. For example, a model for  $n_{HI} = 15 \text{ cm}^{-3}$ , roughly 100 times that of the LIC (Müller *et al.*, 2009), has a TS at 9.8 AU such that Uranus would move in and out of the TS and Neptune would be surrounded by hot, shocked plasma beyond the HP (upwind) or heliotail (downwind). Models of the heliosphere inside a high-speed interstellar wind with corresponding high ram pressure would compress the heliosphere in a similar way. Smith and Scalo (2009) define a “de-screening event” to be a cloud encounter that results in a stellar astrosphere being compressed to less than the size of the star’s habitable zone (defined as the distance from the star where liquid water can be present on a planet’s surface), which they find should happen when a star encounters an interstellar cloud with a number density of  $600(M/M_{\odot})^{-2} \text{ cm}^{-3}$ , where  $M$  is the mass of the star. Only the densest ISM clouds are capable of this de-screening, with such clouds being relatively rare. The densest clouds are cold ( $T \sim 100 \text{ K}$ ) molecular clouds, with many of the refractory elements depleted onto dust grains. In addition to increased GCR exposure (see Ch. 4), a de-screening event caused by a molecular cloud encounter would also expose planetary atmospheres to high fluxes of interstellar dust, with potentially dramatic consequences (Pavlov *et al.*, 2005). In any case, the mass dependence in the above equation leads Smith and Scalo (2009) to conclude that habitable zone planets orbiting stars significantly less massive than the Sun (with spectral types of late K to M) are virtually never exposed to de-screening events, but de-screening may happen occasionally for stars with the Sun’s mass or larger. However, these calculations assumed that the relative velocity of these encounters is only  $10 \text{ km s}^{-1}$ . Assuming a faster encounter speed would increase the estimated frequency of de-screening events.

Fields *et al.* (2008) calculated the first gas dynamic models for the effects of the blast wave from a nearby supernova on the heliosphere assuming the present day properties of the solar wind. Pressure balance between the supernova shock wave and the solar wind produces extreme heliosphere models that have the same physical structures as the Müller *et al.* (2009) models with the heliopause at 1.4 times the distance of the termination shock in the upwind direction but with both located very close to the Sun. Fields *et al.* (2008) find that a supernova located at  $\approx 9 \text{ pc}$  from the Sun would create a heliopause that penetrates to within 1 AU, subjecting the Earth to an infusion of supernova debris including iron and other heavy atoms. The discovery of the radioisotope  $^{60}\text{Fe}$  with a half-life of 1.5 Myr in a deep-sea ferromanganese crust and dated to  $2.8 \pm 0.4 \text{ Myr}$  ago by Knie *et al.* (2004) indicates that a nearby supernova explosion likely occurred only 2.8 Myr ago.

The effect on the Earth of a nearby supernova and the effect on more distant planets from supernovae at distances up to 30 pc will include an increase in the amount of neutral hydrogen atoms, dust, supernova metals, and Galactic Cosmic Rays reaching the planet's atmosphere. The latter would influence the planet's magnetosphere and change the planet's atmospheric chemistry, including the important molecule ozone (see Smith and Scalo, 2009 and references therein).

### 3.6 Detecting astrospheres

The heliosphere is obviously just one example of stellar wind/ISM interaction available for study. All stars with winds will have analogous astrospheres around them. Unfortunately, they are not easy to detect. At least for stars with coronal winds like that of the Sun, the only successful astrospheric detection method so far is the Lyman- $\alpha$  detection method illustrated in Fig. 3.7. Other proposed approaches for detecting winds include the search for CX-induced X-ray emission (Wargelin and Drake, 2001) and free-free emission at radio wavelengths (Gaidos *et al.*, 2000), but these methods have not been successful. Figure 3.7 illustrates that the same HST Lyman- $\alpha$  spectrum can be used to study both heliospheric and astrospheric Lyman- $\alpha$  absorption. Table 3.1 lists all the stars with detected astrospheric absorption (Wood *et al.*, 2005, 2014b). All are very nearby. Interstellar H I column densities increase with distance, and at sufficiently large distances the resulting ISM H I absorption becomes too broad to detect astrospheric (or heliospheric) absorption.

The amount of astrospheric Lyman- $\alpha$  absorption will depend on the thickness of the hydrogen wall, and more generally the size of the astrosphere, which is largely determined by the stellar-mass-loss rate. The absorption can therefore be used as a diagnostic of the stellar wind, which is crucial because coronal winds have so far proved impossible to detect directly around other solar-like stars. This topic is discussed in detail in the next section.

Although we are here mostly interested in the astrospheres of cool main-sequence stars like the Sun, with coronal winds like the solar wind, it is worth at least briefly mentioning other types of astrospheres created by stars very different from the Sun with much more massive winds. Red giant stars have cool, slow ( $v_w \sim 30 \text{ km s}^{-1}$ ) winds with  $\sim 10^3$  times the mass-loss rate of the Sun. The winds are easily detected spectroscopically by observing wind absorption features within emission lines formed close to the star, but there is so far only one reported detection of a red giant's wind/ISM interaction. For  $\alpha$  Tau (K5 III), a Mg II absorption feature has been identified as being due to stellar-wind material compressed and heated behind a radiative TS (Robinson *et al.*, 1998; Wood *et al.*, 2007a).

Table 3.1 *Astrospheric detections from Lyman- $\alpha$  absorption*

Star	Spectral type	$d$ (pc)	$v_{\text{ISM}}$ ( $\text{km s}^{-1}$ )	$\theta$ (deg)	$\dot{M}$ ( $\dot{M}_{\odot}$ )	Log $L_X$	Surf. area ( $A_{\odot}$ )
Main-sequence stars							
Sun	G2 V	...	26	...	1	27.30	1
Proxima Cen	M5.5 V	1.30	25	79	< 0.2	27.22	0.023
$\alpha$ Cen	G2 V+K0 V	1.35	25	79	2	27.70	2.22
$\epsilon$ Eri	K2 V	3.22	27	76	30	28.32	0.61
61 Cyg A	K5 V	3.48	86	46	0.5	27.45	0.46
$\epsilon$ Ind	K5 V	3.63	68	64	0.5	27.39	0.56
EV Lac	M3.5 V	5.05	45	84	1	28.99	0.123
70 Oph	K0 V+K5 V	5.09	37	120	100	28.49	1.32
36 Oph	K1 V+K1 V	5.99	40	134	15	28.34	0.88
$\xi$ Boo	G8 V+K4 V	6.70	32	131	5	28.90	1.00
61 Vir	G5 V	8.53	51	98	0.3	26.87	1.00
$\pi^1$ UMa	G1.5 V	14.4	43	34	0.5	28.96	0.97
Evolved stars							
$\delta$ Eri	K0 IV	9.04	37	41	4	27.05	6.66
$\lambda$ And	G8 IV-III+M V	25.8	53	89	5	30.82	54.8
DK UMa	G4 III-IV	32.4	43	32	0.15	30.36	19.4

Spectroscopic diagnostics of astrospheres are useful, but directly perceiving the size and global structure of an astrosphere requires an image. Imaging astrospheres is generally possible only for the largest astrospheres surrounding stars with the most massive or energetic of winds. Examples include pulsar bow shocks, which are a result of relativistic winds emanating from the rapidly rotating neutron stars (e.g., Brownsberger and Romani, 2014). Bow shocks are also observed around some red supergiants, with slow ( $v_w \sim 10 \text{ km s}^{-1}$ ) but very massive winds having  $\sim 10^7$  times the mass-loss rate of the Sun (e.g., Martin *et al.*, 2007; van Marle *et al.*, 2014). Hot stars, with O and B spectral types, have similarly massive winds driven by radiation pressure, which can also lead to visible bow shocks (e.g., Kobulnicky *et al.*, 2010). Finally, a high-density ISM environment can allow an astrosphere to be detectable. An example is shown on the covers of the *Heliophysics* series (lower right-hand side), in which the wind of a very young star is interacting with the high-density nebula from which it has just been born (see, e.g., Bally *et al.*, 2006, for more information).

### 3.7 Long-term evolution of stellar winds

#### 3.7.1 Inferences from short-term solar wind variability

A complete understanding of how winds affect planets and their atmospheres must start with assessments of how stellar winds evolve with time. It is well established

that stellar activity decreases with age (see Vol. III, Ch. 2, and also Ch. 2 in this volume; Ribas *et al.*, 2005). Young stars rotate rapidly and have very active coronae that emit copious X-ray and EUV radiation. This coronal emission declines as stars age and their rotation rates slow down. Therefore, it is natural to expect that the winds emanating from these coronae should evolve significantly as well. One might expect winds to evolve in concert with the coronal emission, because winds originate in stellar coronae. Thus, young stars might be expected to have more massive winds. There is undoubtedly more material heated to coronal temperatures for young, active stars, and therefore more material available to be accelerated into a wind. However, coronal X-ray emission arises from regions of closed magnetic field where the densities are large, while wind emanates along open field lines. Furthermore, coronal X-ray emission from the Sun varies by a factor of 5–10 over the course of the solar activity cycle (Judge *et al.*, 2003), but the solar mass-loss rate of  $\dot{M}_{\odot} = 2 \times 10^{-14} M_{\odot} \text{ yr}^{-1}$  does not vary much on these time scales (Cohen, 2011). Thus, a more active corona clearly does *not* automatically lead to a stronger coronal wind.

On the other hand, active stars might also have substantial mass loss associated with coronal-mass ejections (CMEs). Strong flares on the Sun are usually accompanied by fast CMEs. These CMEs do not account for most of the solar mass loss (cf., Ch. 4), but flare rates and energies are known to increase dramatically with stellar activity. Young, active stars have stronger and more frequent flares (see Ch. 2), meaning that the mass loss associated with flare-associated CMEs could be much higher (although we do not have the means to empirically establish this; cf., Ch. 2).

Drake *et al.* (2013) computed the CME mass-loss rate expected for young, active stars by extrapolating a known correlation between solar-flare energy and CME mass to more-active stars with more-frequent and energetic flares. The resulting prediction is shown in Fig. 3.9, implying that the most active stars with X-ray luminosities  $L_X \sim 3 \times 10^{30} \text{ erg s}^{-1}$  (compared with  $L_X \sim 2 \times 10^{27} \text{ erg s}^{-1}$  for the Sun) could have mass-loss rates of  $2 \times 10^4 \dot{M}_{\odot}$  due to CMEs alone, although limits on the percentage of a star's bolometric luminosity  $L_{bol}$  that can reasonably be expected to be converted to flares and CMEs ( $\sim 10^{-3} L_{bol}$ ) lead Drake *et al.* (2013) to suggest a lower ceiling of  $2500 \dot{M}_{\odot}$ . However, this prediction of a strong wind for young, active stars is only valid if the solar flare-energy/CME-mass connection can actually be extrapolated to more active stars.

### 3.7.2 Inferences from stellar observations

Observations are required to truly establish how winds evolve with time. Currently, the only way coronal winds can be detected around other stars is through astrospheric Lyman- $\alpha$  absorption, but the number of astrospheric Lyman- $\alpha$  detections is

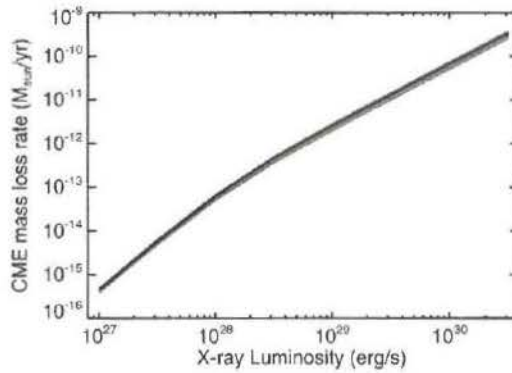


Fig. 3.9 Plausible stellar mass-loss rate due to CMEs as a function of coronal X-ray luminosity, computed by assuming that the solar-flare/CME–mass correlation can be extrapolated to younger, more active stars. Note that the solar X-ray luminosity is  $L_X \sim 2 \times 10^{27} \text{ erg s}^{-1}$ . (From Drake *et al.*, 2013.)

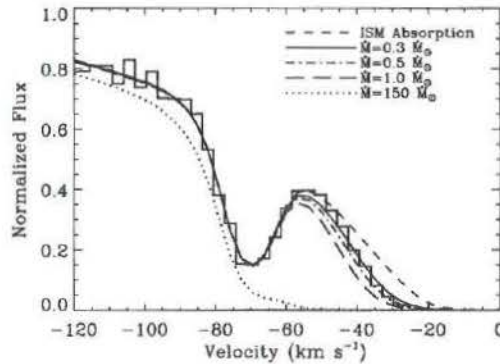


Fig. 3.10 The blue side of the Lyman- $\alpha$  absorption line of  $\pi^1$  UMa, plotted on a heliocentric velocity scale. The absorption at  $-70 \text{ km s}^{-1}$  is from interstellar D I. Because the ISM absorption cannot explain all of the H I absorption, the excess is assumed to be from the stellar astrosphere. The astrospheric absorption signature is compared with absorption predictions from four hydrodynamic models of the astrosphere, assuming four different mass-loss rates for  $\pi^1$  UMa (after the astrospheric absorption is added to that of the ISM). (From Wood *et al.*, 2014b.)

still very limited. Table 3.1 provides the complete list. Among these stars, the best analog for a very young Sun is  $\pi^1$  UMa, a 500 Myr old G1.5 V star. Figure 3.10 shows the Lyman- $\alpha$  spectrum for  $\pi^1$  UMa, zooming in on the blue side of the line where the astrospheric absorption is detected. The amount of absorption correlates with the strength of the stellar wind, but extracting a stellar mass-loss rate from the Lyman- $\alpha$  data requires the assistance of hydrodynamic models of the astrosphere, such as the one in Fig. 3.11.

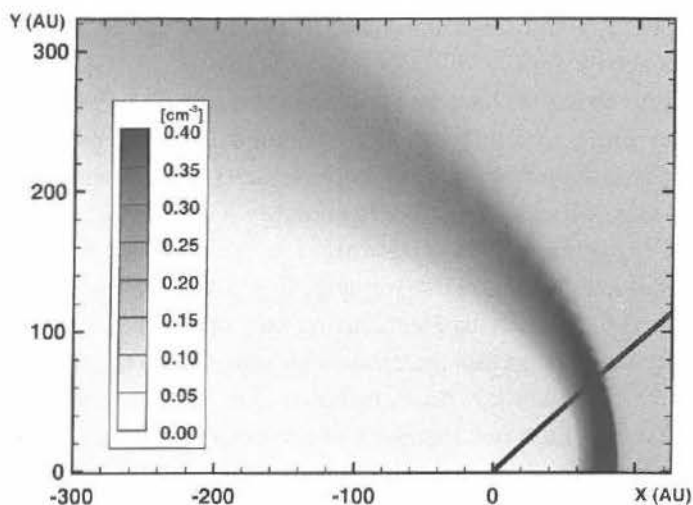


Fig. 3.11 The H I density distribution of a hydrodynamic model of the  $\pi^1$  UMa astrosphere, assuming  $\dot{M} = 0.5\dot{M}_{\odot}$ , which leads to the best fit to the data in Fig. 3.10. The star is at the origin, and the ISM is flowing from the right in this figure. The “hydrogen wall” is the parabolic shaped high-density region stretching around the star. The black line indicates our line of sight to the star. (From Wood *et al.*, 2014b.)

Astrospheric models like that in Fig. 3.11 are extrapolated from a heliospheric model that successfully reproduces heliospheric absorption, specifically a multi-fluid model described by Wood *et al.* (2000). These models assume the same ISM characteristics as the heliospheric model, with the exception of the ISM flow speed in the stellar rest frame,  $v_{\text{ISM}}$ , which can be computed using our knowledge of the local ISM flow vector and each star’s unique space motion vector. Values of  $v_{\text{ISM}}$  are listed in Table 3.1, and  $\theta$  indicates the angle of our line of sight to the star relative to the upwind direction, shown explicitly in Fig. 3.11 for the  $\pi^1$  UMa case.

The astrospheric models are computed assuming different stellar wind densities, corresponding to different mass-loss rates, and the Lyman- $\alpha$  absorption predicted by these models is compared with the data to see which best matches the observed astrospheric absorption. Figure 3.10 shows the astrospheric absorption predicted by four models of the  $\pi^1$  UMa astrosphere, assuming four different stellar mass-loss rates. The model with half the solar mass-loss rate shown in Fig. 3.11 is deemed the best fit to the data (Wood *et al.*, 2014b). Thus, this 500-Myr-old young-Sun analog appears to have a wind comparable in strength to that of the current Sun. Given that  $\pi^1$  UMa is much more active than the Sun, with  $L_X = 9 \times 10^{28} \text{ erg s}^{-1}$ , this implies that the prediction of Fig. 3.9 must be incorrect, meaning that the relation

between flare energy and CME mass seen for the Sun cannot be extrapolated to younger, more active stars.

Mass-loss-rate estimates have been made in this way for all of the astrospheric detections, and Table 3.1 lists these  $\dot{M}$  measurements (Wood *et al.*, 2005, 2014b). Table 3.1 also lists logarithmic X-ray luminosities ( $\log L_X$ ) and surface areas for the observed stars, which can be used to compute X-ray surface flux densities,  $F_X$  (the ratio of X-ray luminosity to surface area). In order to look for some correlation between coronal activity and wind strength, Fig. 3.12 shows mass-loss rates (per unit surface area) plotted versus  $F_X$ , focusing only on the main-sequence stars. For the low-activity stars, mass loss increases with activity in a manner consistent with the  $\dot{M} \propto F_X^{1.34 \pm 0.18}$  power law relation shown in the figure. For the  $\xi$  Boo binary, in which (like  $\alpha$  Cen) the two members of the binary share the same astrosphere, Fig. 3.12 indicates how the binary's combined wind strength of  $\dot{M} = 5\dot{M}_\odot$  is most consistent with the other measurements if 90% of the wind is ascribed to  $\xi$  Boo B, and only 10% to  $\xi$  Boo A.

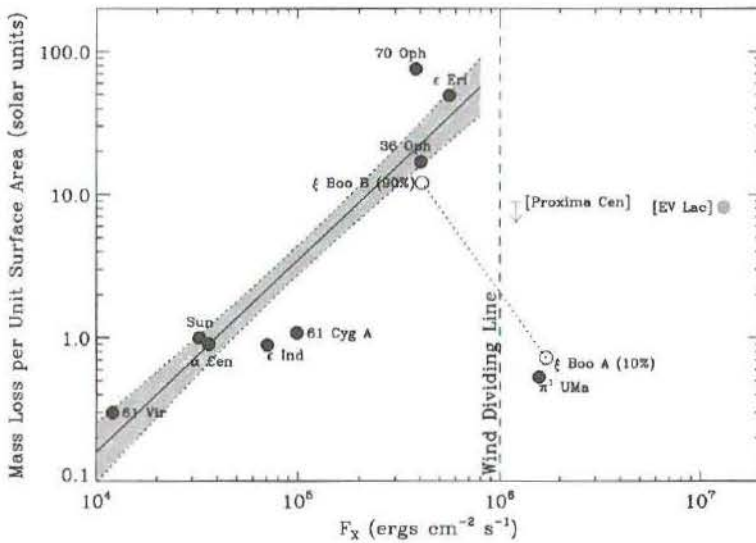


Fig. 3.12 A plot of mass-loss rate (per unit surface area) versus X-ray surface flux density for all main-sequence stars with measured winds. Most of these have spectral types of G (like the Sun) or (cooler) K, but the two with square-bracketed labels are (much cooler) tiny M dwarf stars. Separate points are plotted for the two members of the  $\xi$  Boo binary, assuming  $\xi$  Boo B accounts for 90% of the binary's wind, and  $\xi$  Boo A only accounts for 10%. A power law,  $\dot{M} \propto F_X^{1.34 \pm 0.18}$ , is fitted to the less active stars where a wind/corona relation seems to exist, but this relation seems to fail for stars to the right of the "Wind Dividing Line" in the figure. (From Wood *et al.*, 2014b.)

For  $F_X < 10^6 \text{ erg cm}^{-2} \text{ s}^{-1}$ , mass loss appears to increase with activity. However, above  $F_X = 10^6 \text{ erg cm}^{-2} \text{ s}^{-1}$  (i.e., for more active, and thus generally younger stars) this relation seems to fail, a boundary identified as the “Wind Dividing Line” in Fig. 3.12. Highly active stars above this limit appear to have surprisingly weak winds. This is suggested not only by the two solar-like G stars above the limit,  $\xi$  Boo A and  $\pi^1$  UMa, but also by the two active M dwarfs above the limit, which have very modest mass-loss rates. (For Proxima Cen we only have an upper limit of  $\dot{M} < 0.2\dot{M}_\odot$ , while for EV Lac  $\dot{M} = 1\dot{M}_\odot$ .) The apparent failure of the wind/corona correlation to the right of the “Wind Dividing Line” may indicate a fundamental change in magnetic field topology at that stellar activity level.

It is not easy to study magnetic fields on stars that are unresolvable point sources. Nevertheless, estimates can be made on the basis of empirical stellar age/rotation relations and theoretical magnetic braking models (Schrijver *et al.*, 2003). Sophisticated spectroscopic and polarimetric techniques are also available for studying stellar magnetic fields (Donati and Landstreet, 2009). One interesting discovery is that very active stars usually have stable, long-lived polar starspots (Schrijver and Title, 2001; Strassmeier, 2002), in contrast to the solar example where sunspots are only observed at low latitudes. Perhaps the polar spots are indicative of a particularly strong dipolar magnetic field that envelopes the entire star and inhibits stellar wind flow, thereby explaining why very active stars have surprisingly weak winds. Strong toroidal fields are also often observed for active stars (Petit *et al.*, 2008).

Given that young stars are more active than old stars (e.g., Ribas *et al.*, 2005), the correlation between mass loss and activity indicated in Fig. 3.9 implies an anticorrelation of mass loss with age. Ayres (1997) finds the following relation between stellar X-ray flux and age for solar-like stars:  $F_X \propto t^{-1.74 \pm 0.34}$ . Combining this with the power law relation from Fig. 3.12 yields the following relation between mass loss rate and age:

$$\dot{M} \propto t^{-2.33 \pm 0.55} \quad (3.2)$$

(Wood *et al.*, 2005). Figure 3.13 shows what this relation suggests for the history of the solar wind, and for the history of winds from any solar-like star for that matter. The truncation of the power law relation in Fig. 3.13 near  $F_X = 10^6 \text{ erg cm}^{-2} \text{ s}^{-1}$  leads to the mass-loss/age relation in Fig. 3.13 being truncated as well at about  $t = 0.7 \text{ Gyr}$ . The plotted location of  $\pi^1$  UMa in Fig. 3.13 indicates what the solar wind may have been like at times earlier than  $t = 0.7 \text{ Gyr}$ .

Although winds may have been surprisingly weak for  $t < 0.7 \text{ Gyr}$ , at later times Fig. 3.13 does indicate that solar-like coronal winds can be up to two orders of magnitude stronger than the current solar wind at  $t \approx 1 \text{ Gyr}$ . This makes it more

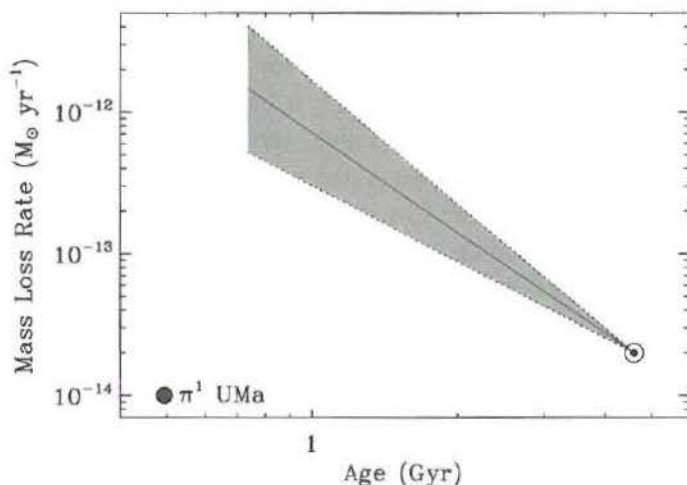


Fig. 3.13 The mass-loss history of the Sun inferred from the power law relation in Fig. 3.12. The truncation of the relation in Fig. 3.12 means that the mass-loss/age relation is truncated as well. The low mass-loss measurement for  $\pi^1$  UMa suggests that the wind weakens at  $t \approx 0.7$  Gyr as one goes back in time. (From Wood *et al.*, 2005.)

likely that the erosive effects of stellar winds play an important role in planetary atmosphere evolution at these later ages (e.g., Luhmann *et al.*, 1992; Lammer *et al.*, 2003; Brain *et al.*, 2010b; Khodachenko *et al.*, 2012).

The wind history suggested by Fig. 3.13 also has relevance for the Faint Young Sun problem (see Vol. III, Ch. 2), which relates to our understanding that at  $t \approx 0.7$  Gyr the Sun would have been  $\sim 25\%$  fainter than today. This would imply temperatures for Earth too cool for liquid water to exist on the surface, inconsistent with our understanding of Earth's geologic history (Sagan and Mullen, 1972). One proposed solution has to do with the possibility that the Sun was at least a few percent more massive in the past, and therefore more luminous (Sackmann and Boothroyd, 2003). This requires a stronger solar wind in the past to allow it to lose that excess mass. Figure 3.13 does indicate a generally stronger solar wind in the past, but not strong enough, unfortunately, as the cumulative solar mass loss suggested by Fig. 3.13 is only  $\sim 10^{-3} M_{\odot}$ , at least an order of magnitude too low. Alternative explanations involving a stronger greenhouse effect may instead be required to resolve the Faint Young Sun problem (Kasting and Ackerman, 1986; see also Chs. 2 and 11 in Vol. II).

In closing, we note that our current understanding of stellar wind and astrosphere evolution for Sun-like stars is relying heavily on a relatively small number of detections of astrospheric Lyman- $\alpha$  absorption. More detections of such absorption will hopefully become available in the future. But there is also a need to

explore completely different ways of studying winds and astrospheres. The Atacama Large Millimeter/submillimeter Array (ALMA) may provide detections of free-free emission from winds, or at least provide much lower upper limits for stellar mass-loss rates. An even more sensitive radio telescope will ultimately be required to directly detect emission from winds as weak as that of the Sun.